Journal of Materials Chemistry A

ROYAL SOCIETY OF CHEMISTRY

PAPER

View Article Online
View Journal | View Issue

Cite this: J. Mater. Chem. A, 2025, 13, 22903

Deciphering the local structure of Prussian blue analogue cathodes with Raman spectroscopy for sodium-ion batteries†

Krishnakanth Sada, Siddhartha Nanda, Hadi Khani and Arumugam Manthiram *

Received 19th March 2025
Accepted 3rd June 2025

DOI: 10.1039/d5ta02248g

rsc.li/materials-a

Iron-based Prussian blue analogues (PBAs) have gained attention as low-cost, relatively higher-potential cathodes for sodium-ion batteries, due to their open 3D-framework structures. However, understanding the local structural changes is critical to unveiling the intercalation pathways and degradation mechanisms. We employ here *operando* Raman spectroscopy to probe the changes in the cyanide vibrational modes during cycling and degradation after cycling, which are not adequately resolved by X-ray diffraction due to the low structure factor and limited X-ray sensitivity of the cyanide groups. Vibrational spectroscopy has thus proven essential for deciphering these complex materials. Additionally, we implement pre-sodiation strategies to assess the impact of sodium inventory loss by pairing PBAs with a hard carbon anode in a full-cell configuration. *Operando* galvanostatic electrochemical impedance spectroscopy (EIS) and *ex situ* X-ray photoelectron spectroscopy (XPS) further elucidate the interface evolution and the role of water molecules in forming the cathode-electrolyte interphase (CEI) and solid-electrolyte interphase (SEI). The insights gained advance the understanding of PBAs and enhance their practical viability.

Introduction

Sodium-ion batteries (SIBs) are appealing as an alternative to lithium-ion batteries (LIBs) for large-scale energy storage due to the high abundance and low cost of sodium.[1–3] The widespread availability of sodium resources across continents presents a significant advantage compared to LIBs. However, SIBs face a penalty of lower energy density and lack of suitable high-energy cathode materials. Prussian blue analogues (PBAs) have attracted attention due to their high theoretical capacities ($\sim$170 mA h g^{-1}) and facile, scalable synthesis. PBAs have the general formula $AM_1[M_2(CN)]_y\square_{1-y}\cdot xH_2O$, where A = Na and $M_1 = M_2$ = Fe, and $\square$ represents the hexacyanometallate $[M_2(CN)_6]$ vacancies.[4] These vacancies significantly impact the kinetics, structural stability, electrochemical performance, and capacity. Synthesizing 100% vacancy-free materials is highly challenging due to the spontaneous growth kinetics and the use of water as a synthesis medium, which allows water molecules to occupy these vacancies.[5,6] There are three different types of water molecules (surface, interstitial, and crystal) present in PBAs, unique to this class of cathodes. Recently, some controlled synthetic strategies have produced highly crystalline materials. However, it is worth noting that a perfect crystalline structure may compromise the diffusion of sodium-ions.[7,8]

PBAs have demonstrated their significance as cathode materials, with CATL announcing the first commercialization of Na-ion batteries utilizing PBAs as well as significant efforts by companies like Natron Energy (USA) and Altris AB (Sweden) extending beyond LIBs.[9,10] Recently, the Group 1ai unveiled their 18 650 K-ion batteries featuring a Prussian blue cathode.[11] Despite these advancements, a considerable gap remains in understanding the local structure and degradation pathways of these cathodes. The low scattering factor of carbon and nitrogen atoms, coupled with the inability of powder X-ray diffraction (PXRD) to detect changes in the framework due to its low sensitivity to lighter atoms (lower electronic cloud), presents a challenge. Additionally, PXRD averages diffraction signals across the entire sample (exposed to X-rays), making it difficult to capture localized structural changes, such as bond bending or tilting.[12] To address these limitations, we conduct here a comparative study with *operando* Raman spectroscopy and X-ray diffraction to investigate the vibrational mode changes in the CN groups. While the role of water molecules in PBAs has been extensively documented earlier by our group[13] and other studies,[6,14–16] it is equally evident that complete

Materials Science and Engineering Program, Walker Department of Mechanical Engineering, The University of Texas at Austin, Austin, Texas 78712, USA. E-mail: manth@austin.utexas.edu

† Electronic supplementary information (ESI) available: Detailed procedure for synthesis and characterization; *operando* Raman spectroscopy; XPS; structure factor differences between C, N and Fe; Raman representation table; XPS Fe spectra with detailed tabulation; hard carbon electrochemistry; and PITT. See DOI: https://doi.org/10.1039/d5ta02248g

removal of interstitial water molecules induces structural strain and a synchronized motion of Fe–$(CN)_6$ octahedra.

In this work, we investigate the local structural changes of $[Na_2Fe[Fe(CN)_6]\cdot 1.69H_2O$ (NFF) with *operando* Raman spectroscopy and XRD for the first two cycles and *operando* Raman spectroscopy after 100 cycles to understand the structural changes during cycling. Both the hydrated monoclinic phase (M-NFF) and the dehydrated rhombohedral phase (R-NFF) are synthesized with a controlled acid decomposition method to obtain a low concentration of vacancies. We also assess the cycling performance of the cathodes in a full cell configuration with a hard carbon anode. The hard carbon anode was pre-sodiated to understand the sodium inventory loss during cycling. The interfacial chemistry is also probed with X-ray photoelectron spectroscopy (XPS) on the electrodes at charged and discharged states. In addition, *operando* galvanostatic electrochemical impedance spectroscopy is performed to monitor the real time growth of interfacial resistance.

Results and discussion

Electrochemical performance with the pre-sodiation strategy

In our recent study, we explored the controlled synthesis of low-vacancy and high-quality PBA cathodes through an acid decomposition of sodium ferrocyanide in mild hydrochloric acid (HCl) (ESI Note1†).[13,17,18] The precipitated sodium iron hexacyanoferrate ($Na_2Fe[Fe(CN)_6]\cdot 1.69H_2O$, NFF) was thoroughly washed and dried overnight under vacuum at 80 °C before being transferred to an argon-filled glove box (H_2O < 0.1 ppm and O_2 < 0.1 ppm). The X-ray diffraction patterns of both the hydrated and dehydrated samples are presented in Fig. S1.† The synthesized material, containing interstitial water molecules, possesses a monoclinic structure (space group $P2_1/c$). Drying the M-NFF above ~200 °C overnight under vacuum successfully removed the interstitial water molecules, inducing a co-operative tilting of the octahedra and modifying the interactions among Na, cyanide (–C≡N–) and transition-metal (TM) centers. This dehydration process transformed the material from monoclinic to rhombohedral structure (space group $R\bar{3}$). As these materials are synthesized in water medium, careful electrode processing is essential to acquire good electrochemical performance, so we prepared the electrodes inside the glove box to avoid the complications associated with surface water molecules.[13,19] Electrochemical characterization of these cathodes was conducted by paring with hard carbon (HC) anodes. To minimize complications associated with the HC anode, commercial HC electrodes were procured from MTI. These anodes were pre-sodiated with direct-contact methods to mitigate the first cycle irreversibility and enhance sodium-ion inventory. This process involved laminating electrodes with an artificial solid-electrolyte interphase (SEI) on pre-sodiated electrodes, as evidenced by scanning electron microscopy (SEM, Fig. S2†). Energy-dispersive X-ray spectroscopy (EDS) mapping confirmed the sodium-rich artificial SEI, which contributes to the stable cycling of the electrodes while also preserving sodium inventory. The optimal pre-sodiation time was determined by assembling HC||Na half-cells and evaluating the first-cycle coulombic efficiency (ESI, Fig. S3†).

The cycling performances of both M-NFF and R-NFF were evaluated with an electrolyte consisting of 1 M $NaPF_6$ in a 1 : 1 (v/v) mixture of ethylene carbonate (EC) : diethyl carbonate (DEC) with 3% fluoroethylene carbonate (FEC) additive (Fig. 1). The M-NFF sample exhibits a sloping charge–discharge profile with an average operating voltage of 2.8 V and a specific capacity of ~85 mA h g^{-1}. The initial three formation cycles were performed between 3.8 and 1.3 V at C/20 rate, followed by cyclability tests between 3.7 and 1.3 V at C/5 rate. Fig. 1a presents the voltage profiles of M-NFF up to 200 cycles, including the first 3 cycles and one representative cycle for every 10 cycles. The sample demonstrates good cycling stability, retaining more than 85% of the initial capacity (Fig. 1b). A clear variation in the average voltage is observed in the charge–discharge profiles. The average potential drop calculated over 200 cycles reveals an increase from 0.1 to 0.4 V. Notably, the average potential drop is more pronounced during the discharge process, approximately 200 mV higher compared to the charge process (Fig. 1c). The differences in the average potentials may include the contribution from the hard carbon anode as well. Despite this, the pre-sodiation approach ensures favorable first-cycle coulombic efficiencies. Similarly, the electrochemical performance of R-NFF was evaluated by paring with the pre-sodiated HC anode. The dehydrated phase exhibits two distinguishable plateaus: a sloping region at 2.75 V associated with high-spin Fe–N (HS-Fe_N) and a plateau at 3.24 V corresponding to low-spin Fe–C (LS-Fe_C). The voltage profiles for R-NFF are shown in Fig. 1d, displaying the first three cycles and then one representative cycle every 10 cycles.

To gain deeper insights into the intercalation behavior of R-NFF, potentiostatic intermittent titration technique (PITT) measurements were performed. The HS-Fe_N process exhibits no change in the current (red curve), characterized by a sloping voltage profile, while the LS-Fe_C redox couple at higher voltages shows a variation in current that represents a bell-shaped curve (red color) with a distinct plateau (ESI Note 2, Fig. S4†). R-NFF demonstrates an initial capacity exceeding ~150 mA h g^{-1} at a C/20 rate, maintaining approximately 75% of its initial capacity after 100 cycles and ~60% after 200 cycles (Fig. 1e) at the rate of C/5. The average voltage drop over 200 cycles reveals a more significant drop during the discharge process compared to the charge process, consistent with the observations with M-NFF (Fig. 1f). However, R-NFF exhibits a more uniform voltage drop, which is ~200 mV lower than that of M-NFF. The rate capabilities of the full cells were evaluated across current rates ranging from C/20 to 2C (Fig. 1g and h). The cells maintain good coulombic efficiencies at different current rates, with the second-cycle charge–discharge profiles for each rate shown in Fig. S5.† R-NFF exhibits a significant capacity variation of ~25 mA h g^{-1} between 1C and 2C rates, possibly due to severe particle pulverization and kinetic limitations associated with the biphasic reaction.

Influence of ligands on the redox energies

PBAs are intriguing crystal systems, featuring both high-spin and low-spin transition-metal redox centers. Understanding the

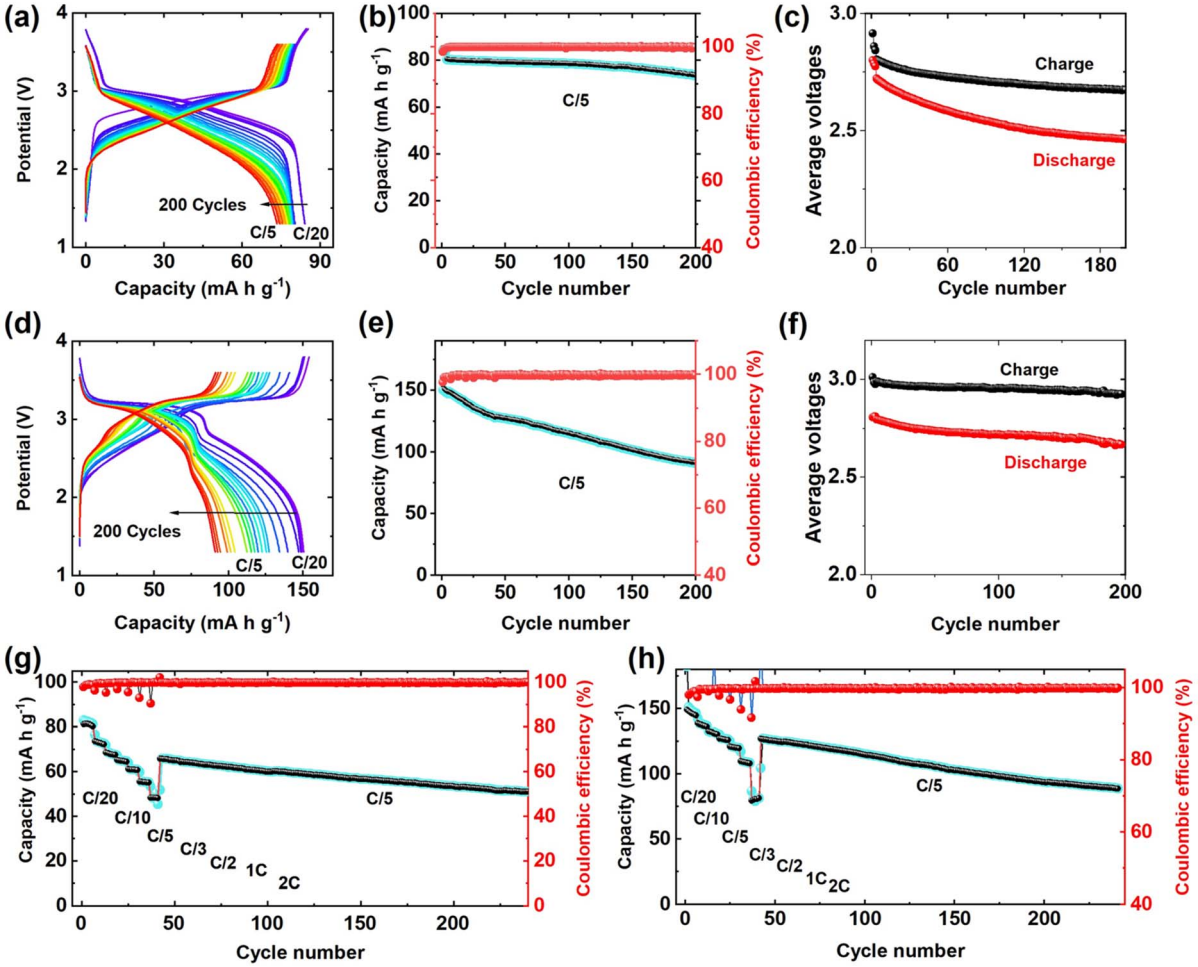

Fig. 1 Electrochemical performance evaluations of both M-NFF and R-NFF: (a) galvanostatic voltage profiles of M-NFF over 200 cycles. (b) Cycling stability of M-NFF at a C/5 rate up to 200 cycles. (c) Average potential variation in the charge–discharge curves. (d) Galvanostatic voltage profiles of R-NFF over 200 cycles. (e) Cycling stability of R-NFF at a C/5 rate up to 200 cycles; (f) average potential variation of the charge–discharge curves. Rate performance of (g) M-NFF and (h) R-NFF, with the potentials referenced with respect to the hard carbon anode.

redox energies associated with them can provide valuable insights into the redox mechanisms in PBA systems and can be extended to other PBA compositions. Polyanionic materials are well-known for their ability to tune redox potentials through the inductive effect.[20,21]

In $Na_2Fe[Fe(CN)_6]\cdot xH_2O$, the Fe redox centers are bridged by cyanide ligands. One Fe atom is bonded to six carbon atoms, forming FeC_6 octahedra associated with low-spin Fe (LS-Fe_C), while the other Fe is bonded to six nitrogen atoms, forming FeN_6 octahedra associated with high-spin Fe (HS-Fe_N). The stronger ligand field strength in FeC_6 due to the more covalent Fe–C bonds causes a larger crystal field splitting, resulting in a low spin configuration. On the other hand, the weaker ligand field strength arising from relatively less covalent Fe–N bonds causes a smaller crystal field splitting, resulting in a high-spin configuration. The redox energies associated with low-spin and high-spin $Fe^{2+/3+}$ and the consequent cell voltages associated with them are schematically illustrated in Fig. 2.

Fig. 2a and b presents the voltage profiles of both the hydrated and dehydrated NFFs with the insets showing the normalized dQ/dV curves. The profiles show a comparison between the half-cell and full-cell configurations for both the hydrated and dehydrated sodium iron hexacyanoferrate. However, the influence of interstitial water molecules becomes evident in the voltage profile of the hydrated monoclinic ($P2_1/c$) M-NFF.[13] The strong interaction between water molecules and Na^+ ions produces a sloping profile with a distinguishable lower redox feature at 2.8 V. The higher voltage redox process is further split into multiple peaks, as observed in the black curve of the M-NFF half-cell configuration. This is possibly due to the side reactions associated with water molecule interaction with the electrolyte. The dehydrated sample provides almost the same capacity and similar profiles in both versions of cell assembly. The lower plateau exhibiting a sloping behavior may originate from the hard carbon anode. Fig. 2c and d presents the rhombohedral and monoclinic crystal structures, respectively, with $\frac{1}{4}$ of a single unit cell to see the differences in bonding connectivity and the out-of-plane rotation of the octahedra in the R-NFF structure due to the removal of water molecules. The inset in the figure presents the representation of

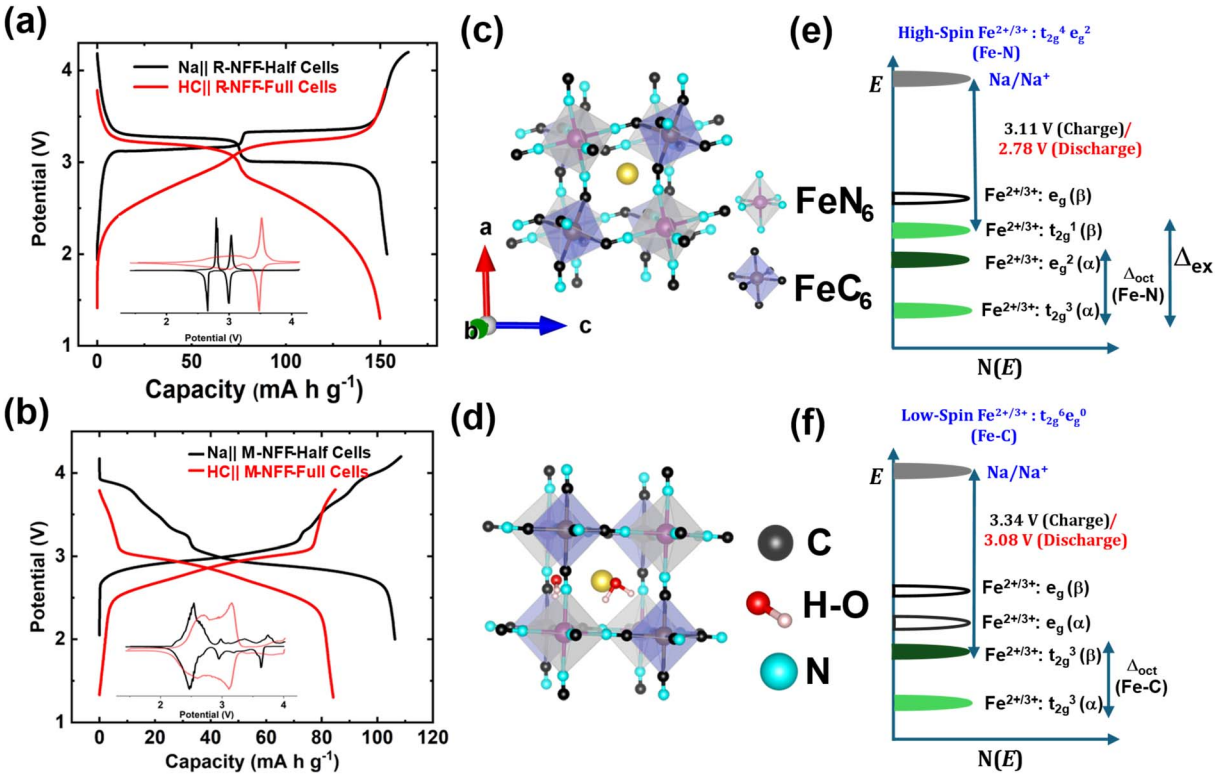

Fig. 2 Comparison of the charge/discharge profiles and redox energies of both M-NFF and R-NFF: (a) cycling profiles of R-NFF in both the full cell and half-cell configurations. (b) Cycling profiles of M-NFF in both full cell and half-cell configurations. (c) Rhombohedral crystal structure. (d) Monoclinic crystal structure. Energy levels of the t_{2g} and e_g bands for (e) high-spin Fe^{2+} and (f) low-spin Fe^{2+}. Δ_{oct} refers to octahedral-site crystal field splitting and Δ_{ex} refers to exchange energy when pairing the electrons in the same orbital. The symbols α and β refer to, respectively, up-spin and down-spin electrons, with Δ_{ex} representing the energy difference between them.

different atoms. The monoclinic structure in Fig. 2d is very close to the cubic structure. However, a small tilt in the C–N bond results in a change in one of the bond angles to $\beta = 92°$. Fig. 2e and f give the energy levels of the t_{2g} and e_g bands for high-spin Fe^{2+} and low-spin Fe^{2+}, respectively, in octahedral sites. Whether Fe^{2+} will adopt a high-spin or low-spin configuration depends on the relative magnitudes of the crystal field splitting Δ_{oct} and the exchange energy Δ_{ex}, which is the energy cost when two electrons occupy the same orbital.

Probing the intercalation mechanisms with *operando* Raman spectroscopy *vs. operando* X-ray diffraction

Operando Raman spectroscopy was conducted to investigate the vibrational mode changes during the cycling process. Numerous studies, including our recent work,[13] have explored sodium-ion intercalation mechanisms in both the hydrated and dehydrated phases. While *operando* X-ray diffraction (XRD) has been instrumental in revealing the bulk structural transformations, its sensitivity to local structural changes is limited due to variations in the overall structure factor (refer to the atomic form factor *vs.* scattering angle curves of C and N in Fig. S6†). In contrast, *operando* Raman spectroscopy can provide a more nuanced understanding of the local coordination environments. Especially, the –CN– stretching band is highly sensitive to Na-driven structural changes in PBA. The room-temperature *operando* Raman spectra of M-NFF and R-NFF (Fig. 3) clearly highlight the differences in their charge storage mechanisms. M-NFF undergoes a simple and highly reversible monoclinic to cubic phase transition when the Na-ion content drops below 1.5 per formula unit. Fig. 3a compares the second cycle plot of *operando* Raman and XRD, illustrating this reversible transformation.

To better understand the subtle local structural changes, the vibrational modes in the Raman spectra were deconvoluted at different states-of-charge (SOC). In the lower wavenumber region (200–600 cm^{-1}), the vibrational modes between 400 and 600 cm^{-1} correspond to Fe–C stretching, while the modes near 200 cm^{-1} represent Fe–CN–Fe bond deformation.[22] In the higher wavenumber region (2000–2200 cm^{-1}), the two intense vibrational modes were deconvoluted to four distinguishable modes. Based on our recently published findings,[13] the monoclinic structure of M-NFF with C_{2h} site symmetry exhibits Raman-active modes at 2096 and 2125 cm^{-1} (colored red), corresponding, respectively, to the B_g and A_g modes. Rietveld refinement of the XRD data of M-NFF identified Fe atoms occupying the low symmetry (4*e*) and high symmetry (2*d*) Wyckoff positions, indicating a partial difference in oxidation states between Fe atoms. The literature also attributes the B_g and A_g modes to Fe^{2+}–CN–Fe^{3+} configurations. Additionally, the shoulder modes at 2080 and 2107 cm^{-1} (colored pink) are

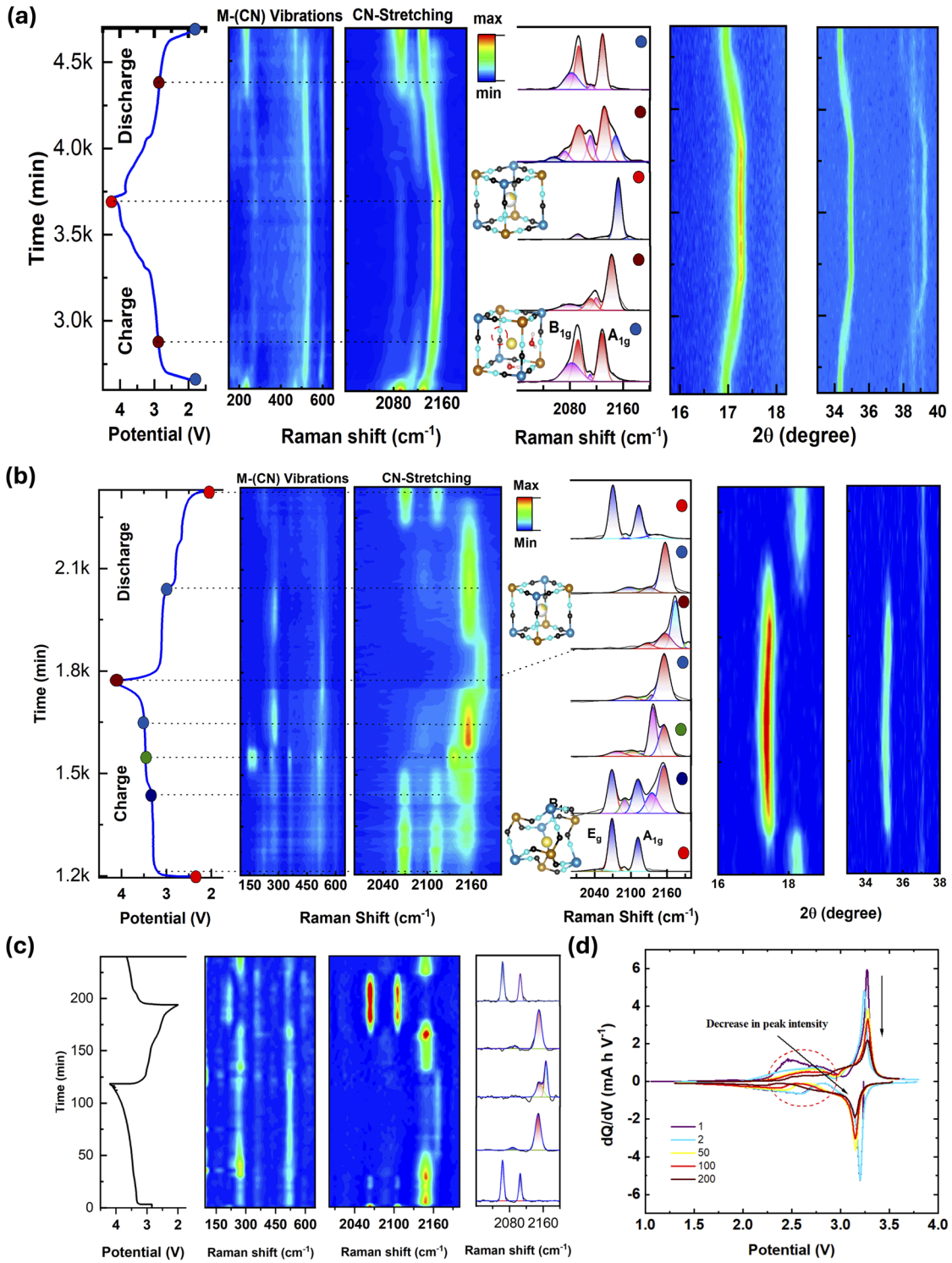

Fig. 3 Comparison of both *operando* Raman and XRD in the second cycle: (a) M-NFF with 2D contour maps with similar structural information and (b) R-NFF with 2D contour maps exhibiting differences. Raman spectra showing local vibrational changes upon charging to higher voltages. (c) *Operando* Raman contour map of R-NFF after 100 cycles and (d) charge–discharge profiles of R-NFF at the 2nd, 50th and 100th cycles in the half-cell configuration, presenting the gradual disappearance of the high-spin Fe redox couple.

characteristic of Fe^{2+}–CN–Fe^{2+} vibrations, as previously reported in the literature.[23–25] Here, the authors reported the presence of low-spin Fe^{2+}, high spin Fe^{2+}, and high spin Fe^{3+} in monoclinic Prussian blue by virtue of Mössbauer spectroscopy. These observations provide critical insights into the complex charge storage mechanisms and local structural transformations within PBAs during electrochemical cycling.

The presence of conformational changes (variations in the spatial arrangement of atoms or linkages within the existing framework) in the –CN– bridge between the two Fe^{2+} centers is not detectable by *operando* XRD, highlighting the importance of *operando* Raman spectroscopy. Further, the presence of Fe^{3+} could be attributed to oxidation during synthesis or a small fraction of vacancies. The charge–discharge curves show a distinct plateau at ~2.8 V, which corresponds to the redox reaction associated with HS-Fe_N. Notably, the high-spin Fe^{2+} bonded to nitrogen is oxidized first as its redox level lies at a higher energy compared to that of low-spin Fe^{2+} bonded to carbon (Fig. 2). This behavior is also reflected in the *operando* Raman spectra: during charge, the vibrational modes associated with Fe^{2+}–CN–Fe^{2+} disappear, while those corresponding to Fe^{2+}–CN–Fe^{3+} undergo a blue shift with an increase in intensity, indicating the oxidation of HS-Fe_N. Interestingly, in the same plateau region, we also start to see the oxidation of LS-Fe_C, which results in the formation of Fe^{3+}–CN–Fe^{3+} and represents an incomplete oxidation of HS-Fe_N. Previously, it has been reported that the incomplete oxidation of HS-Fe_N is due to the bonding between HS-Fe_N and water that prevents complete oxidation.[25] In the cubic phase, the NFF framework adopts an ideal O_h symmetry, exhibiting three Raman active modes: A_{1g}, E_g, and T_{1u} [refer to the ESI notes for detailed calculations, Table S1†]. The T_{1u} and T_{2u} modes are Raman-inactive. The A_{1g} mode, representing the symmetric stretching and compression of C≡N bonds, results in a constructive addition of bond polarizability components, producing a sharp intense vibrational mode at higher wavenumbers. Conversely, the E_g mode represents asymmetric stretching and manifests as a lower-intensity mode at lower wavenumbers (~2090 cm^{-1}).[26] This description aligns well with the observed Raman modes at the end of charge (red dot); particularly, the two modes at 2156 and 2090 cm^{-1} (colored blue) are characteristic of the Fe^{3+}–CN–Fe^{3+} configuration, indicating a complete oxidation of LS-Fe_C as well as HS-Fe_N. Rietveld refinement[13] further supports these observations, showing that Fe atoms in the cubic phase occupy the high symmetry 4*a* and 4*b* Wyckoff positions, both possessing $m\bar{3}m$ site symmetry.[27] This symmetry implies that both Fe atoms share the same oxidation state (+3) in the cubic phase, consistent with the Raman spectroscopic observations.

In the lower wavenumber region, the ~200 cm^{-1} mode disappears at the onset of charge and reappears during the final stages of discharge. This could be due to the structural changes from monoclinic to cubic, with the Fe–CN–Fe bond deformation seizing to exist due to a straightening of Fe–CN–Fe (in cubic) from the oriented/deformed Fe–CN–Fe (in monoclinic). The ~500 cm^{-1} mode, representing the Fe–C stretching, undergoes a blue shift with an increase in intensity during charge, indicating a bond strengthening as Fe is oxidized. This comprehensive analysis of Raman spectra provides valuable insights into the deintercalation mechanisms, summarized below.

$$\{Fe^{2+}\text{–CN–}Fe^{2+} + Fe^{2+}\text{–CN–}Fe^{3+}\}\ (\text{monoclinic}) \rightarrow Fe^{2+}\text{–CN–}Fe^{3+}\ (\text{low intensity}) + Fe^{3+}\text{–CN–}Fe^{3+}\ (\text{sharp intensity with shifted peaks}) \rightarrow Fe^{3+}\text{–CN–}Fe^{3+}\ (\text{cubic}).$$

During discharge at 3 V (brown dots), we see five major peaks in the higher wavenumber region. The two sharp peaks in red at 2096 and 2130 cm^{-1} correspond to Fe^{2+}–CN–Fe^{3+} configurations, while the two peaks in pink at 2072 and 2110 cm^{-1} are characteristic of Fe^{2+}–CN–Fe^{2+} vibrations and the peak in blue at 2152 cm^{-1} shows the presence of a small fraction of Fe^{3+}–CN–Fe^{3+}. However, at the end of discharge (blue dots), this peak has completely disappeared. Hence the intercalation mechanism can be summarized as below:

$$Fe^{3+}\text{–CN–}Fe^{3+}\ (\text{cubic}) \rightarrow Fe^{3+}\text{–CN–}Fe^{3+} + Fe^{2+}\text{–CN–}Fe^{3+} + Fe^{2+}\text{–CN–}Fe^{2+} \rightarrow \{Fe^{2+}\text{–CN–}Fe^{3+} + Fe^{2+}\text{–CN–}Fe^{2+}\}\ (\text{monoclinic})$$

The modes at the lower wavenumber region exhibit a similar trend and clearly change with phase transformation. The vibrations at 210 cm^{-1} are observed at the onset of charge below 2.8 V and during discharge below 3.0 V. Even after complete charge at 4.2 V, the Raman modes corresponding to the cubic phase persist similar to the observations in the higher wavenumber. In contrast, XRD does not exhibit the same sensitivity as Raman spectroscopy, although it does reveal the phase transformation from monoclinic to cubic. The *operando* Raman spectra in the first cycle, presented in Fig. S7,† further support this observation.[28] These vibrational modes provide insights into the origin of the changes in the number of modes associated with the monoclinic and cubic phases. In the cubic phase, the –C≡N– bond behaves as a linear entity with simple symmetric vibrations, whereas an increase in the number of vibrations is observed with symmetry disruption.

R-NFF serves as an excellent example to demonstrate the superior sensitivity of Raman spectroscopy for probing local structures in Prussian blue analogues compared to *operando* XRD. The *operando* XRD data presented in Fig. 3b illustrate phase transitions from rhombohedral to cubic structure, accompanied by an ~18% volume expansion. For R-NFF, the initial Raman modes correspond to the rhombohedral phase ($R\bar{3}$ space group, C_{3i} point group) with modes located at 2060 and 2120 cm^{-1}, assigned to E_g and A_{1g}, respectively, based on our previous study.[13] These two peaks are characteristic of Fe^{2+}–CN–Fe^{2+} vibrations.[23] This is further supported by the Rietveld refinement of the rhombohedral phase, which indicates that Fe atoms occupy the 3*a* and 3*b* Wyckoff positions with identical symmetry, implying the same oxidation state. As the charging progresses, new vibrational modes are observed near the end of the first plateau (~3.2 V in the charge–discharge profile, Fig. 3b; first cycle presented in Fig. S8†). The two modes at 2096 and 2125 cm^{-1} represent Fe^{2+}–CN–Fe^{3+} indicating an oxidation of HS-Fe_N. The peak at 2156 cm^{-1}, characteristic of cubic NFF, corresponds to the A1g mode and Fe^{3+}–CN–Fe^{3+} vibrations, signifying the onset of LS-Fe_c oxidation. Further charging at ~3.5 V leads to a complete disappearance of Fe^{2+}–CN–Fe^{2+} modes and the emergence of sharp vibrational modes for Fe^{2+}–CN–Fe^{3+} and Fe^{3+}–CN–Fe^{3+}. Just before the charging process concludes, a pure cubic phase is observed, characterized by sharp, intense Fe^{3+}–CN–Fe^{3+} vibrational modes.

Interestingly, at the end of charge, the low intensity Fe^{3+}–CN–Fe^{3+} modes and a sharp vibrational mode at ~2173 cm^{-1} are observed. Previously, Wang *et al.* reported the presence of a tetragonal phase under extremely sodium-deficient conditions.[29,30] Also, Goodenough's group demonstrated that the tetragonal phase ($P4/_{mmm}$) exhibits a lower volume compared to the cubic phase with *ex situ* PXRD investigation.[15] This newly observed Raman mode at higher wavenumbers at the end of charge is likely indicative of a tetragonal phase due to its lower volume compared to that of the cubic phase and higher symmetry compared to that of the rhombohedral phase. Such subtle local structural changes are not detected by *operando* XRD studies. As previously mentioned, the presence of water molecules in M-NFF alters the local interactions between Na, CN, and transition-metal sites, resulting in a higher initial Fe^{3+} content. Consequently, the tetragonal phase is not observed with M-NFF, as a larger amount of Na can be extracted from R-NFF compared to that from M-NFF. Similar cubic-to-tetragonal phase transitions have been reported due to lattice mismatches and induced strain.[31] In the R-NFF system, the extremely Na-deficient cubic phase at 4.2 V exhibits significant internal strain, triggering a transition to the tetragonal phase to alleviate this strain. Upon discharge, the reappearance of the modes at 2060 cm^{-1} and 2120 cm^{-1} confirms the reversible restoration to the rhombohedral structure. The lower wavenumber region presents a more complex scenario. In the rhombohedral structure, the Fe–C≡N–Fe units are significantly distorted and oriented along the [111] axis due to Na^+ displacement, leading to complex motions and prominent Raman modes. Assigning these modes requires phonon vibrational calculations, which are beyond the scope of this study.

Throughout the *operando* studies, we have observed asymmetric behavior during charge and discharge, suggesting the Na^+ intercalation behavior is different. Similar behavior has been previously reported and has been attributed to various factors, such as the presence of an H_2O molecule at certain sites blocking the Na^+ pathway, a change in coulombic interaction between negatively and positively charged species during Fe redox reactions, and different strain behaviors due to structural changes, which in turn can affect the Na^+-ion diffusion.[32,33] In Fig. 3a and b, colored dots are used to indicate the state of charge corresponding to the deconvoluted spectra, enabling a correlation between state of charge and the phase transitions observed. The Raman spectra associated with discharge in Fig. 3b exhibit a hump at a higher wave number due to undischarged residues.

Earlier studies by Nielsen *et al.*[34] confirmed that the long-term cycling stability is affected primarily by the loss of sodium inventory rather than structural changes, as observed through synchrotron XRD after multiple cycles with different potential cut-offs. In this study, we aimed to gain insights into the local structure by monitoring the changes in the –CN vibrational modes, which are more sensitive and responsive to local structural variations. These observations lead us to conclude that the capacity fade associated with R-NFF is not exclusively due to sodium inventory loss but also involves local structural changes.

To further investigate the changes in the vibrational modes indicative of potential structural degradation over time due to reversible sodium-ion insertion and extraction, we conducted *operando* Raman spectroscopy after 100 cycles. Interestingly, the *operando* Raman spectra of M-NFF exhibit minimal noticeable changes even after prolonged cycling, suggesting that peak shifts are gradual and largely reversible, as observed during the initial cycles (Fig. S9†). In contrast, significant changes are evident in the Raman spectra and discharge plateaus of the dehydrated R-NFF sample. As shown in Fig. 3c, the Raman spectra reveal three clearly distinguishable modes. Initially, the peaks at 2067 and 2110 cm^{-1} correspond to the E_g and A_{1g} modes observed in the rhombohedral phase ($R\bar{3}$ space group). These two peaks exhibit slight shifts compared to those observed during the initial cycles, indicating the presence of strain and disorder in the system due to continuous reversible phase transitions. Upon further charging, a cubic phase emerges with two peaks at 2156 and 2083 cm^{-1}, corresponding to the A_{1g} and E_g normal modes. Additionally, the sodium-deficient tetragonal phase reported in the literature begins to emerge much earlier, at around 3.4 V (corresponding to $x = 0.6$) with a peak at 2164 cm^{-1}.

As discussed above, a Na-poor phase induces strain that promotes the transition from the cubic to tetragonal phase. After 100 cycles, the system accumulates intrinsic strain, making this phase transition thermodynamically favorable, resulting in an early emergence of the tetragonal phase alongside a reduced cubic phase fraction. The long-term cycling stability test reveals a gradual reduction in the contributions from the high-spin Fe phase, as evidenced by the disappearance of the charge plateau at 3.11 V (decrease in the peak intensity in the dQ/dV plot). This degradation contributes to a significant reduction in cell capacity, which decreases from ~150 to < 92 mA h g^{-1} after 200 cycles (see Fig. 1d and the derivative curve in Fig. 3d). These findings suggest a potential structural transformation driven by strain-induced cooperative octahedral tilting. Previous studies have reported that extensive cycling leads to sodium inventory loss due to side reactions during formation cycles and the formation of the SEI on the anode, which results in distinct *operando* Raman profiles and diminished capacity.[34] Thus, the use of vibrational spectroscopy provides valuable insights into the local structural dynamics of these complex systems.

Operando impedance spectroscopy

Operando galvanostatic electrochemical impedance spectroscopy (GEIS) was employed to delineate the growth of internal resistance as a function of SOC. A full-cell architecture with negligible influence from the hard carbon anode was considered to better understand the kinetics and the development of interfacial resistance. A symmetric cell comprising pristine HC and charged HC was assembled, and its resistance was measured to evaluate the contributions from HC and is presented in Fig. S10.† The equivalent-circuit model (refer to the inset in Fig. 4a) consists of three different resistance components (R_s, R_{SEI}, and R_{ct}), two constant-phase elements or non-

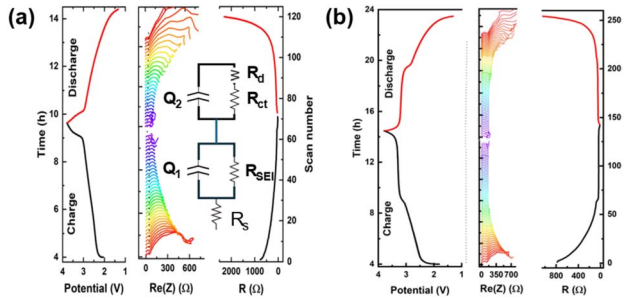

Fig. 4 *Operando* GEIS. (a) M-NFF *vs.* HC: first cycle charge–discharge profiles and Nyquist impedance plots recorded every five minutes, along with the calculated impedance (the inset corresponds to the equivalent-circuit diagram). (b) R-NFF *vs.* HC: first cycle charge–discharge profiles in comparison with GEIS measurements.

ideal capacitive elements (Q_1 and Q_2), and one Warburg diffusion element (R_d).[35] The impedance spectra were collected every five minutes to ensure collection of the data in the span of the near-equilibrium-state of the system. The analysis enabled the observation of changes in each component at various SOC levels. R_s, representing contact resistance, reflects the adhesion of the active material with the current collector and the quality of electrical contacts within the cell. R_{SEI} refers to the SEI or passive layer formed during the cycling process. The effect of both R_s and R_{SEI} remained constant or negligible throughout the study, although these values are higher for M-NFF compared to that for R-NFF.

Fig. 4 shows the changes in the electrochemical impedance during cycling. At an initial SOC of 0%, the systems exhibit a high charge-transfer resistance, with values of 752 Ω for R-NFF and 782 Ω for M-NFF. As the deintercalation process progresses, the charge-transfer resistance decreases in both M-NFF and R-NFF. The hydrated sample consistently demonstrates higher resistance than the dehydrated sample, indicating superior conductivity for the dehydrated phase. *Operando* EIS measurements clarify the influence of Na-ion concentration on diffusion kinetics within the structure. Initially, both the resistance and Na-ion concentration are relatively high. As the Na-ion concentration decreases, the resistance also decreases, exhibiting a similar trend during the discharge process.

Probing the interface compositions with X-ray photoelectron spectroscopy (XPS)

We sought to understand the interphases formed during cycling on both the electrodes, CEI on the cathode and SEI on the anode for both M-NFF and R-NFF. To achieve this, high-resolution X-ray photoelectron spectroscopy (XPS) was employed to investigate the valence states of Fe, surface species, and their compositional variations, particularly focusing on the influence of water molecules. While XPS is inherently surface sensitive, depth profiling can be performed by sputtering to analyze the bulk composition of the sample. This technique provides critical insights into the chemical and electronic states of the elements, aiding in the understanding of the interfacial processes. Since the role of water molecules in the interphase formation is crucial, XPS measurements were conducted on both the cathode and anode after the initial charge and discharge cycles to elucidate their impact on the electrochemical performance (Fig. 5 and 6). Fig. 5a illustrates the changes in the oxidation states of Fe at different SOCs and after three minutes of sputtering, which helps assess depth-related changes. Since XPS is a surface-sensitive technique, sample preparation is critical; the samples were loaded into an air-sensitive holder inside a glove box to prevent contamination or changes by reacting with the atmosphere and then transferred to the XPS equipment without exposure to the atmosphere.

The Fe 2p XPS spectra exhibit characteristic peaks at 721.2/721.9 and 708.5/709.3 for R-NFF, corresponding to Fe^{2+}/Fe^{3+} $2p_{1/2}$ and Fe^{2+}/Fe^{3+} $2p_{3/2}$, respectively. Similarly, for M-NFF, the peaks were observed at 721.1/721.8 and 708.7/709.5, indicating the presence of Fe^{2+}/Fe^{3+} in the Na-rich phases of the PBAs, with a dominant fraction of Fe^{2+} (82.3%) and a smaller fraction of Fe^{3+} (<10%).[29,36,37] Upon charging, Fe^{2+} undergoes oxidation to Fe^{3+}, resulting in a mixed valence state of Fe^{2+} and Fe^{3+}. The emergence of a distinct satellite (shake-up) peak at 715.1 eV, associated with the Fe^{3+} oxidation state of R-NFF, further confirmed the participation of Fe in the redox process. This satellite peak became significantly prominent in the charged electrodes, accounting for more than 60% of the spectral area. Interestingly, surface analysis of M-NFF after three minutes of sputtering revealed no significant changes in the Fe spectrum. In contrast, R-NFF exhibited an increased concentration of Fe^{3+}, as indicated by the prominent peak at 710.5 eV. This difference explains the large capacity disparity between R-NFF and M-NFF. M-NFF demonstrates limited oxidation and partial participation in the reaction, resulting in a lower capacity of ~80 mA h g^{-1}, whereas R-NFF exhibits a higher capacity of ~150 mA h g^{-1}. The discharged electrodes confirm the reduction of Fe^{3+} back to Fe^{2+}.

Even after three minutes of sputtering, no substantial spectral changes were observed. M-NFF shows a progressive reduction to Fe^{2+} with a minor fraction of residual Fe^{3+}. The electronic environments of Fe $2p_{3/2}$ and Fe $2p_{1/2}$ are influenced by electronegativities, wherein an increase in electron donation from the carbon s-orbital to Fe, indicated by a higher wavenumber in vibrational spectroscopy ν(C≡N), enhances the electron density on the Fe center. This increase in electron density is reflected in the reduced binding energy of the Fe $2p_{3/2}$ peak and an increased bond strength of ν(C≡N) upon charge (ν > 2165 for R-NFF, Fig. 3b), signifying a shift in the electronic environment of Fe. The peak positions, binding energy differences, and intensity ratio (I_{ratio}, defined as ($I_{FeII\ 2p3/2\ main}$)/($I_{FeIII\ 2p3/2\ main}$)), along with the satellite intensity ratio ($I\_{ratio\ satel}$, defined as ($I_{Fe\ 2p3/2\ satel}$)/($I_{Fe\ 2p3/2\ main}$)), are tabulated in the ESI (Table S2†). The charge transfer detected by XPS can be related to ν(C≡N), which serves as a measure of the σ-bond strength. Satellite peaks, found in all samples at a few eV above the main Fe $2p_{3/2}$ peak, correspond to charge-transfer interactions between Fe and CN ligands. Larger satellite peaks indicate an increased charge transfer (electron density) from the ligand to the metal.[38] The satellite intensity ratio serves as a quantitative

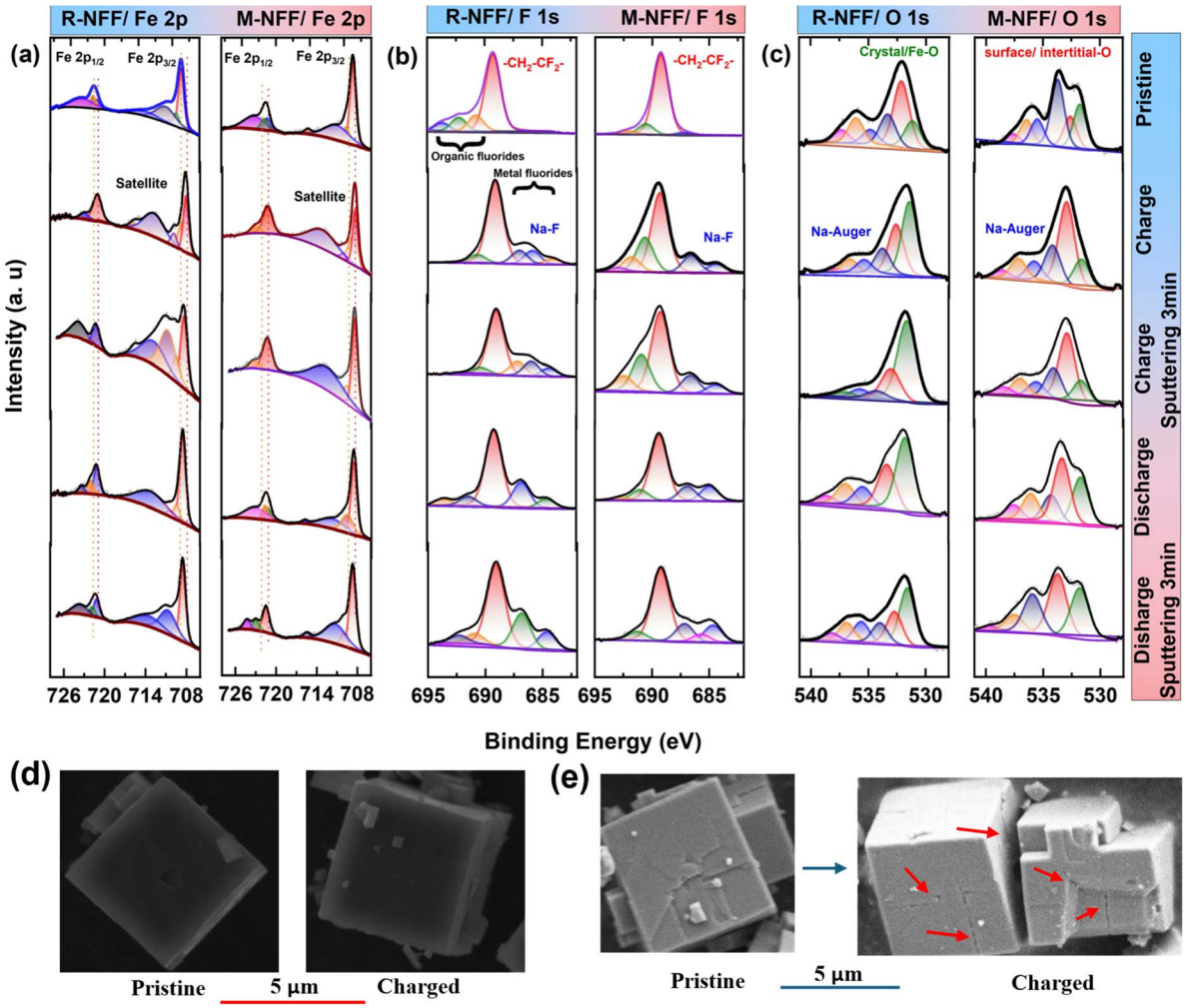

Fig. 5 XPS and SEM analyses: (a) Fe 2p region in R-NFF and M-NFF, comparing the surface and subsurface states after the charge–discharge processes and also following 5 min of sputtering, (b) F 1s region, distinguishing organic and inorganic fluoride compositions, and (c) O 1s region, revealing the role of water molecule interactions. (d) SEM image of an M-NFF particle before and after charging and (e) SEM image of R-NFF before and after charging, highlighting the formation of cracks in the particles.

indicator of charge transfer; the greater the satellite peak intensity, the greater is the electron density transfer from C≡N to Fe.

During the electron-transfer processes, such as XPS photoemission, the sample undergoes inner-sphere reorganization to stabilize the positively charged species formed. This structural reorganization is associated with the changes in the coordination geometry or bond distances within the complex. The oxidation of the Fe-metal center (Fe^{2+} to Fe^{3+}) involves simultaneous electronic transitions and vibrational excitations. In this process, the wavenumber and binding energy are directly proportional, while the variations in ν(C≡N) serve as an indicator of inner-sphere reorganization energy. Overall, the Fe XPS measurements provide two key insights: first, Fe oxidation is consistent with the observed capacities of both cathodes; second, the presence of water molecules might play a role in incomplete oxidation of M-NFF. The stronger attraction of Na–(OH_2) with a reorganization of Na ions can prevent complete oxidation of Fe^{2+}. Additionally, the possible formation of oxygen-rich species, such as Fe $(OH)_3$ or Fe_2O_3, could contribute to the formation of irreversible passivation layers.[39] The satellite peaks are more expressive in the charged states than in the discharged states and are located at around 713 eV in R-NFF. Similarly, they are located at 713.5 eV in the charged electrodes and 711 eV in discharged electrodes in M-NFF. Further, the peak separation between Fe $2p_{3/2}$ and Fe $2p_{1/2}$ deviates from the ideal 13.6 eV, which further attests to the influence of interstitial and crystal water molecules on the cathodes.

To further investigate the bonding interactions within the CEI, the F 1s and O 1s regions in the XPS were analyzed with pristine, charged, discharged materials and after three minutes of sputtering (Fig. 5b and c). F 1s spectra reveal a primary peak at 689.2 eV, indicative of organic fluorides. Notably, the pristine spectra for both R-NFF and M-NFF differ significantly from those of the charged and discharged electrodes.

The initially present organic fluoride bonds, originating from the binder, were deconvoluted into quartet peaks for R-NFF at 689.2, 690.7, 692.4 and 693.9 eV, and for M-NFF at 687.0,

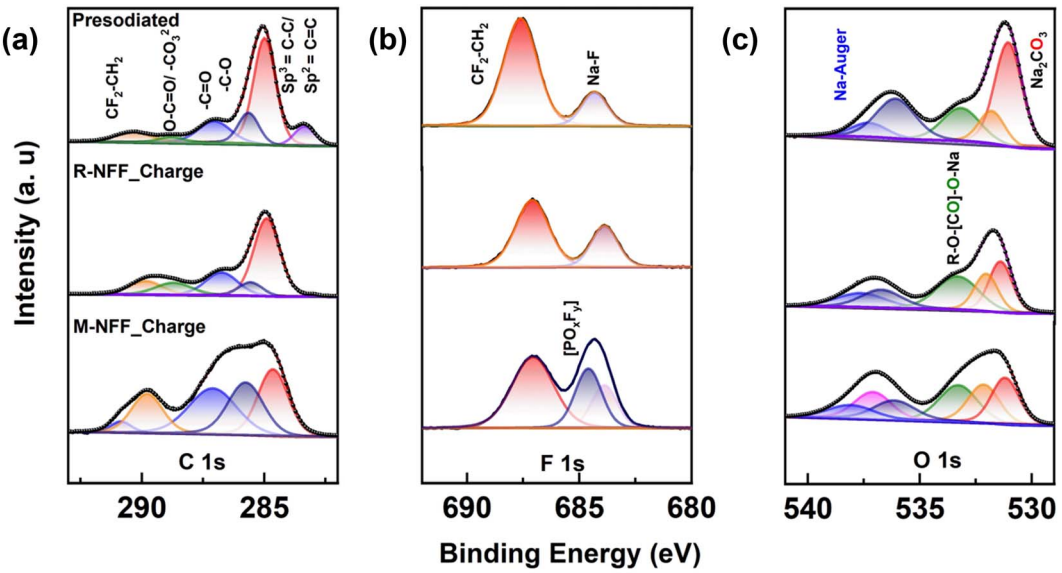

Fig. 6 XPS data of the hard carbon anode: (a) C 1s region has sp^3 and sp^2 binding interactions and oxygen rich carbonates, indicating the presence of both organic and inorganic compositions. (b) F 1s region shows the formation of stronger metal fluoride bonds due to the formation of the artificial SEI on pre-sodiated electrodes. (c) XPS of the O 1s region.

689.2, 690.6, and 692.2 eV. Upon charging, the fluoride bond shifts toward binding energies associated with metal-fluoride interactions. Differences between the R-NFF electrodes before and after sputtering suggest the formation of a thin CEI layer. In contrast, M-NFF maintains consistent fluoride bonding interactions, with peaks corresponding to organic fluorides above 688 eV and metal fluorides near 685 eV. This stability is attributed to a stable CEI with the presence of FEC additive. The O 1s spectra demonstrate clear distinctions between the dehydrated and hydrated electrodes. R-NFF exhibits intense peaks at 532.1 eV, corresponding to surface/interstitial water in the pristine compound and the peak at 531.1 signifies the Fe–O bond. The Na Auger peaks appear above 536 eV in both R-NFF and M-NFF. In contrast, M-NFF displays different spectral features due to the involvement of oxygen atoms from structural water molecules.[13] The spectra were deconvoluted into three distinct peaks corresponding to surface water (533.8 eV), interstitial water (532.7 eV), and lattice or crystalline water (531.7 eV). The pristine sample has more surface water molecules, and during the charge and discharge processes, interstitial water interactions became dominant, with broad peaks observed at 532.7 eV.[29,40] The interstitial water molecules migrate to the surface due to strong Na–OH_2 interactions, shifting the peaks to higher binding energies (533 eV) after sputtering. The O 1s spectra clearly highlight the structural involvement of water molecules in the formation of the CEI. They also signify the interaction of the interstitial water molecule and its role in the hydrated NFF phase.

Despite the pronounced role of water in CEI formation, M-NFF exhibits more stable cycling compared to R-NFF, with a difference exceeding 9% in first-cycle coulombic efficiency. This deteriorated performance is attributed to the significant volume change (~18%) associated with the phase transformation of R-NFF from a rhombohedral to cubic structure, exposing new facets to the electrolyte and leading to constant electrolyte consumption. SEM data (Fig. 5d and e) reveal significant cracking in the charged electrode particles of R-NFF, whereas no such damage is observed in M-NFF. The resulting strain likely exposes new facets to the electrolyte, contributing to continuous electrolyte consumption, formation of resistive interfaces, and consequent long-term instability.

Understanding the SEI on the surface of hard carbon can provide valuable insights into stable cycling performance, crossover of transition-metal ions, and the primary components of the SEI at different states of the charge–discharge process. Accordingly, the cells were made with commercial hard carbon electrodes paired with PBA cathodes with a homemade electrolyte comprising 1 M $NaPF_6$ in EC : DEC with 3% FEC additive. The pre-sodiation strategy ensured the formation of a stable and fluoride rich SEI. Fig. 6 presents the deconvoluted XPS spectra for C 1s, F 1s, and O 1s, comparing the pre-sodiated electrodes with the charged electrodes of both R-NFF and M-NFF, and the discharged states are presented in the ESI (Fig. S11 and S12†). The C 1s spectra show typical sp^2 C=C and sp^3 C–C peaks at lower binding energies of < 284 eV. Carbonate species, including various C–O, C=O, and CO_3^{2-} species, are observed at 285, 287 and 288 eV. The pre-sodiated electrode contains more organic components possibly due to the strongly bonded organic electrolytes.

The FEC additive contributes to the formation of stable fluoride-rich species at the interface, such as CF_2–CH_2, which appears at around 292 eV (Fig. 6b). Both R-NFF and M-NFF have rich C–O species. However, M-NFF paired with HC contains dominant oxygen species –C=O at 287 eV, which may be linked to the increasing resistance at the interface and presence of water molecules. The F 1s spectra further clarify the formation

of a fluoride-rich interface, with Na–F (685.83 eV) and CF_2–CH_2 (689.06 eV) species present. These peaks remain at the same binding energies for the pre-sodiated hard carbon electrodes and R-NFF. However, in M-NFF, the peak positions shift by ~1.01 eV in both charged and discharged electrodes (Fig. 6b). The FEC additive facilitates the formation of a stable inorganic Na–F layer on the electrode surface, which protects the hard carbon and prevents further electrolyte decomposition.[41,42] Fig. 6c shows the deconvoluted O 1s spectra, with peaks identified at 533.17 eV (Na_2CO_3), 534.95 eV (R–O–(CO)O–Na), and 538.67 eV (Na-Auger) in the pristine electrodes.

Fig. S13† illustrates the role of polytetrafluoroethylene (PTFE) as structural binder, functioning similar to a gabion basket to facilitate the formation of a free-standing sheet during the fabrication of self-standing electrodes. Additionally, we have conducted EDS analysis and elemental mapping of these electrodes presented in Fig. S14 and 15.† The pre-sodiated electrode was also analyzed with EDS and elemental mapping and presented in Fig. S16.† It reveals a uniform distribution of the CEI and SEI components in the electrodes.

Conclusions

In this work, a comprehensive investigation of the local structural changes was carried out during the insertion/extraction of Na ions into/from PBA cathodes, with the aid of vibrational spectroscopy. The findings demonstrate that X-ray diffraction lacks sensitivity to detect subtle structural changes due to the low scattering factors of carbon and nitrogen atoms. In contrast, *operando* Raman spectroscopy conducted during the initial charge–discharge cycling (1st and 2nd cycles) as well as after the 100th cycle clarified that capacity fade in the dehydrated R-NFF is not solely due to Na inventory loss, but also results from local structural changes. Furthermore, *operando* electrochemical impedance spectroscopy (EIS) revealed resistance dependence on Na ion concentration. Analysis of the interfacial chemistry with XPS indicated the presence of oxygen-rich species in the hydrated phases, suggesting the release of water molecules from the lattice. This observation implies that Na-rich phases are more resistive and less conductive. Overall, as suggested in our previous study, the introduction of small molecules with less interactions in the place of water is recommended to maintain the open framework of the PBA structure. This strategy can reduce structural strain during cycling and facilitate a faster diffusion kinetics, thereby enhancing long-term electrochemical performance.

Data availability

The datasets generated during and/or analyzed during the current study are available from the authors on reasonable request.

Conflicts of interest

The authors declare no conflicts of interest.

Acknowledgements

This work was primarily supported by the U.S. Department of Energy, Office of Basic Energy Sciences, Division of Materials Science and Engineering under award number DE-SC0005397. H. K and S. N. acknowledge the funding provided by the U.S. Department of Energy, Advanced Research Projects Agency for Energy (ARPA-E) under the EVs4ALL program (award number: DE-AR00001723, work authorization number: 22/CJ000/07/03) for part of the Raman spectroscopy work. The authors thank Dr Hugo Celio for his assistance with collecting the XPS data.

Notes and references

1 A. Rudola, A. J. R. Rennie, R. Heap, S. S. Meysami, A. Lowbridge, F. Mazzali, R. Sayers, C. J. Wright and J. Barker, *J. Mater. Chem. A*, 2021, **9**, 8279–8302.
2 A. Rudola, R. Sayers, C. J. Wright and J. Barker, *Nat. Energy*, 2023, **8**, 215–218.
3 K. Sada, J. Darga and A. Manthiram, *Adv. Energy Mater.*, 2023, **13**, 1–22.
4 J. Cattermull, M. Pasta and A. L. Goodwin, *Mater. Horiz.*, 2021, **8**, 3178–3186.
5 P. S. Camacho, R. Wernert, M. Duttine, A. Wattiaux, A. Rudola, P. Balaya, F. Fauth, R. Berthelot, L. Monconduit, D. Carlier and L. Croguennec, *ACS Appl. Mater. Interfaces*, 2021, **13**, 42682–42692.
6 I. Nielsen, A. Ulander, F. Juranyi, S. R. Larsen, M. Karlsson, W. R. Brant and M. S. Andersson, *Chem. Mater.*, 2024, **36**, 11246–11253.
7 W. R. Brant, R. Mogensen, S. Colbin, D. O. Ojwang, S. Schmid, L. Häggström, T. Ericsson, A. Jaworski, A. J. Pell and R. Younesi, *Chem. Mater.*, 2019, **31**, 7203–7211.
8 H. L. B. Boström and W. R. Brant, *J. Mater. Chem. C*, 2022, **10**, 13690–13699.
9 A. Bauer, J. Song, S. Vail, W. Pan, J. Barker and Y. Lu, *Adv. Energy Mater.*, 2018, **8**, 1702869.
10 K. Wu, X. Dou, X. Zhang and C. Ouyang, *Engineering*, 2022, **21**, 36–38.
11 **https://group1.ai**.
12 A. Rafalska-Łasocha, K. Podulka and W. Łasocha, *Powder Diffr.*, 2011, **26**, 39–47.
13 K. Sada, S. M. Greene, S. Kmiec, D. J. Siegel and A. Manthiram, *Small*, 2024, **20**, 2406853.
14 I. Nielsen, D. Dzodan, D. O. Ojwang, P. F. Henry, A. Ulander, G. Ek, L. Häggström, T. Ericsson, H. L. B. Boström, W. R. Brant and J. Phy, *Energy*, 2022, **4**, 044012.
15 J. Song, L. Wang, Y. Lu, J. Liu, B. Guo, P. Xiao, J. J. Lee, X. Q. Yang, G. Henkelman and J. B. Goodenough, *J. Am. Chem. Soc.*, 2015, **137**, 2658–2664.
16 J. Cattermull, K. Sada, K. Hurlbutt, S. J. Cassidy, M. Pasta and A. L. Goodwin, *Chem. Mater.*, 2022, **34**, 5000–5008.
17 W. R. Brant, R. Mogensen, S. Colbin, D. O. Ojwang, S. Schmid, L. Häggström, T. Ericsson, A. Jaworski, A. J. Pell and R. Younesi, *Chem. Mater.*, 2019, **31**, 7203–7211.
18 C. Q. X. Lim and Z. K. Tan, *ACS Appl. Energy Mater.*, 2021, **4**, 6214–6220.

19 F. M. Maddar, D. Walker, T. W. Chamberlain, J. Compton, A. S. Menon, M. Copley and I. Hasa, *J. Mater. Chem. A*, 2023, **11**, 15778–15791.
20 A. Gutierrez, N. A. Benedek and A. Manthiram, *Chem. Mater.*, 2013, **25**, 4010–4016.
21 L. Wang, J. Song, R. Qiao, L. A. Wray, M. A. Hossain, Y. De Chuang, W. Yang, Y. Lu, D. Evans, J. J. Lee, S. Vail, X. Zhao, M. Nishijima, S. Kakimoto and J. B. Goodenough, *J. Am. Chem. Soc.*, 2015, **137**, 2548–2554.
22 G. Moretti and C. Gervais, *J. Raman Spectrosc.*, 2018, **49**, 1198–1204.
23 L. Ge, Y. Song, P. Niu, B. Li, L. Zhou, W. Feng, C. Ma, X. Li, D. Kong, Z. Yan, Q. Xue, Y. Cui and W. Xing, *ACS Nano*, 2024, **18**, 3542–3552.
24 R. Mažeikien, G. Niaura and A. Malinauskas, *J. Electroanal. Chem.*, 2011, **660**, 140–146.
25 Z. Wang, M. T. Sougrati, Y. He, P. N. L. Pham, W. Xu, A. Iadecola, R. Ge, W. Zhou, Q. Zheng, X. Li and J. Wang, *Nano Energy*, 2023, **109**, 108256.
26 S. F. A. Kettle, G. L. Aschero, E. Diana, R. Rossetti and P. L. Stanghellini, *Inorg. Chem.*, 2006, **45**, 4928–4937.
27 M. I. Aroyo, *International Tables for Crystallography*, International Union of Crystallography, Chester, England, 2016, vol. A.
28 H. Li, J. Huang, K. Yang, Z. Lu, S. Yan, H. Su, C. Liu, X. Wang and B. Ren, *J. Phys. Chem. Lett.*, 2022, 479–485.
29 W. Wang, Y. Gang, J. Peng, Z. Hu, Z. Yan, W. Lai, Y. Zhu, D. Appadoo, M. Ye, Y. Cao, Q. F. Gu, H. K. Liu, S. X. Dou and S. L. Chou, *Adv. Funct. Mater.*, 2022, **32**, 1–13.
30 W. Wang, Y. Gang, Z. Hu, Z. Yan, W. Li, Y. Li, Q.-F. Gu, Z. Wang, S.-L. Chou, H.-K. Liu and S.-X. Dou, *Nat. Commun.*, 2020, **11**, 980.
31 R. Fukaya, M. Nakajima, H. Tokoro, S. Ohkoshi and T. Suemoto, *Phys. Status Solidi B*, 2011, **248**, 482–485.
32 E. Lee, D. E. Brown, E. E. Alp, Y. Ren, J. Lu, J. J. Woo and C. S. Johnson, *Chem. Mater.*, 2015, **27**, 6755–6764.
33 Z. Zhang, M. Avdeev, H. Chen, W. Yin, W. H. Kan and G. He, *Nat. Commun.*, 2022, **13**, 7790.
34 I. Nielsen, C. A. Hall, A.-M. Mattsson, R. Younesi, A. Buckel, G. Ek and W. R. Brant, *J. Mater. Chem. A*, 2024, **12**, 17413–17421.
35 L. U. Subasinghe, G. Satyanarayana Reddy, A. Rudola and P. Balaya, *J. Electrochem. Soc.*, 2020, **167**, 110504.
36 M. C. Biesinger, B. P. Payne, A. P. Grosvenor, L. W. M. Lau, A. R. Gerson and R. S. C. Smart, *Appl. Surf. Sci.*, 2011, **257**, 2717–2730.
37 T. U. Wi, C. Park, S. Ko, T. Kim, A. Choi, V. Muralidharan, M. Choi and H. W. Lee, *Nano Lett.*, 2024, **24**, 7783–7791.
38 S. J. Gerber and E. Erasmus, *Mater. Chem. Phys.*, 2018, **203**, 73–81.
39 D. O. Ojwang, M. Svensson, C. Njel, R. Mogensen, A. S. Menon, T. Ericsson, L. Häggström, J. Maibach and W. R. Brant, *ACS Appl. Mater. Interfaces*, 2021, **13**, 10054–10063.
40 Y. J. Oh, J. J. Yoo, Y. Il Kim, J. K. Yoon, H. N. Yoon, J. H. Kim and S. Bin Park, *Electrochim. Acta*, 2014, **116**, 118–128.
41 S. Komaba, T. Ishikawa, N. Yabuuchi, W. Murata, A. Ito and Y. Ohsawa, *ACS Appl. Mater. Interfaces*, 2011, **3**, 4165–4168.
42 L. Chen, B. Kishore, M. Walker, C. E. J. Dancer and E. Kendrick, *Chem. Commun.*, 2020, **56**, 11609–11612.